Journal of Materials Chemistry B

ROYAL SOCIETY OF CHEMISTRY

PAPER

Cite this: *J. Mater. Chem. B*, 2023, **11**, 2157

Crosslinked albumin–manganese nanoaggregates with sensitized T_1 relaxivity and indocyanine green loading for multimodal imaging and cancer phototherapy†

Ying An,[a] Weiwei Chen,[b] Yiran Li,[a] Hongxia Zhao,[a] Deju Ye,[a] Huipu Liu,[a] Kun Wu[a] and Huangxian Ju *[a]

Received 19th November 2022,
Accepted 28th January 2023

DOI: 10.1039/d2tb02529a

rsc.li/materials-b

Albumin–manganese-based nanocomposites (AMNs) characterized by simple preparation and good biocompatibility have been widely used for *in vivo* T_1-weighted magnetic resonance imaging (MRI) and cancer theranostics. Herein, an aggregation and crosslinking assembly strategy was proposed to achieve the sensitization to T_1 relaxivity of the albumin–manganese nanocomposite. At a relatively low Mn content (0.35%), the aggregation and crosslinking of bovine serum albumin–MnO_2 (BM) resulted in a dramatic increase of T_1 relaxivity from 5.49 to 67.2 mM^{-1} s^{-1}. Upon the loading of indocyanine green (ICG) into the crosslinked BM nanoaggregates (C-BM), the T_1 relaxivity of the C-BM/ICG nanocomposite (C-BM/I) was further increased to 97.3 mM^{-1} s^{-1}, which was much higher than those reported previously even at high Mn contents. Moreover, the presence of C-BM greatly enhanced the photoacoustic (PA) and photothermal effects of ICG at 830 and 808 nm, respectively, and the second near infrared fluorescence (NIR-II FL) of ICG also showed better stability. Therefore, the synthesized C-BM/ICG nanocomposite exhibited remarkable performance in *in vivo* multimodal imaging of tumors, such as T_1-weighted MRI, NIR-II FL imaging and PA imaging, and cancer phototherapy with little side effects. This work provided a highly efficient and promising multifunctional nanoprobe for breaking through the limits of cancer theranostics, and opened a new avenue for the development of high-relaxivity AMNs and multimodal imaging methodology.

Introduction

Magnetic resonance imaging (MRI) has become a powerful and widely implemented imaging technique in medical imageology by virtue of its limitless penetration depth, high spatial resolution, noninvasive and three-dimensional imaging characteristics.[1,2] In terms of *in vivo* T_1-weighted MRI, shorter T_1 relaxation time of protons within a specific area means a brighter MR image.[3] Nevertheless, many pathological tissues that do not have a significant morphological change, and T_1 relaxation time change cannot be distinguished from normal tissues, which greatly limits the application of T_1-weighted MRI in disease diagnosis.[4] To improve the diagnostic accuracy, T_1 contrast agents (CAs) with a superparamagnetic effect are usually applied to shorten the T_1 relaxation time of water protons within pathological tissues, and thus enhance the positive contrast of an MR image. These CAs possess high T_1 relaxivity (r_1, mM^{-1} s^{-1}), defined as the slope of a plot of relaxation rate ($1/T_1$, s^{-1}) *versus* concentration of CAs (mM).[5,6] Generally, the CAs with high T_1 relaxivity can satisfy the required MR contrast at a low dose, which can lower potential biological toxicity.[7] Therefore, the T_1 CAs with higher relaxivity are eagerly desired in T_1-weighted MRI. However, commercially available gadolinium(III)-based CAs often suffer from relatively low relaxivity as well as serious health problems including nephrogenic systemic fibrosis (NSF) and Gd^{3+} deposition in the brain and body.[7,8] Therefore, Gd^{3+}-free alternatives with high relaxivity and long-term safety have attracted considerable attention in recent years. Among the alternatives, manganese-based CAs,[9–11] such as albumin–manganese-based nanocomposites (AMNs), are of low cost, and exhibit negligible biotoxicity, and considerable T_1 relaxivity, thus holding great potential in T_1-weighted MRI.[12] These AMNs with enhanced T_1 relaxation generally consist of albumin–MnO_2 and/or other loadings, in which albumin–MnO_2 is synthesized by reducing $KMnO_4$ with albumin (*e.g.*, bovine serum albumin (BSA), human serum albumin, or ovalbumin).[12]

BSA-MnO_2 (BM), as a typical T_1 contrast agent of AMNs, can be simply prepared by reducing $KMnO_4$ with BSA to produce a

[a] *State Key Laboratory of Analytical Chemistry for Life Science, School of Chemistry and Chemical Engineering, Nanjing University, Nanjing 210023, China. E-mail: hxju@nju.edu.cn*

[b] *School of Geographic and Biologic Information, Nanjing University of Posts and Telecommunications, Nanjing 210023, China*

† Electronic supplementary information (ESI) available: General experiments, supplementary figures, tables and references. See DOI: https://doi.org/10.1039/d2tb02529a

sphere-like morphology with sub-10 nm size.[13,14] The good water-accessibility due to the presence of surface Mn ions and the hydrogen bond interactions between BSA and water molecules result in the impressive T_1 relaxivity of BM. Unfortunately, the reported r_1 value of BM is still at a relatively low level such as 7.9 mM^{-1} s^{-1} (0.5 T)[13] or 5.9 mM^{-1} s^{-1} (0.5 T).[14] Several strategies have been proposed to improve the T_1 relaxivity of BM.[13–16] For instance, the loading of paclitaxel or indocyanine green (ICG) into BM can increase the r_1 to 13.9 mM^{-1} s^{-1} or 70.6 mM^{-1} s^{-1} (0.5 T),[13] and two CAs, PMHN-DA and OMPN, synthesized by integrating polymerization and biomineralization, show the r1 of 38.14 and 31.07 mM^{-1} s^{-1} (0.52 T), respectively.[15,16] Although these improved CAs can basically meet the acquirement for *in vivo* T_1-weighted MRI of pathological tissues, their high-dose usage accompanied by a high Mn content (0.9–3.0%) increases the potential biological toxicity.[17–19] Therefore, new strategies to acquire high-relaxivity AMNs are still in urgent need.

Recently, a self-assembly strategy of paramagnetic small molecules has been developed for the preparation of Gd^{3+}-based nanoassemblies with improved T_1 relaxivity.[20,21] Based on this, an enzyme-mediated *in situ* self-assembly method has also been proposed to develop an activatable pretargeted strategy for Gd^{3+}-based multimodality imaging.[22] These works demonstrate that the formation of Gd^{3+}-based nanoparticles with increased sizes can enhance the T_1 relaxivity at an identical Gd concentration, which is attributed to the prolonged molecule tumbling time.[23,24] Inspired by this phenomenon, this work proposed an aggregation and crosslinking assembly strategy to prepare large-sized BM nanoaggregates (C-BMs) with low Mn content (0.35%) (Scheme 1a), which showed exciting sensitization to T_1 relaxivity of BM.

To achieve the multimodal imaging of tumor tissues and cancer therapy, C-BMs were further used for loading of ICG with the second near infrared fluorogenic (NIR-II FL), photoacoustic (PA) and phototherapeutic characteristics, which are predictable to enhance the T_1 relaxivity of C-BMs as previously reported.[13] Interestingly, the presence of C-BMs not only improved the NIR-II FL stability of ICG, but also boosted the photoacoustic effect of ICG, providing a powerful nanoprobe (C-BM/I) for NIR-II FL and photoacoustic imaging. In addition, C-BMs also enhanced the photothermal (PT) effect of ICG, which is beneficial to cancer therapy (Scheme 1a). Thus, the loading of ICG into C-BM produced a merit of "1 + 1 > 2", and resulted in a protocol for *in vivo* T_1-weighted MRI, NIR-II FL imaging (NIR-II FLI), PA imaging (PAI) of tumours and cancer phototherapy including photothermal therapy (PTT) and photodynamic therapy (PDT) (Scheme 1b). Using both H460 lung cancer cells and H460 tumor-bearing mice as models, the C-BM/I nanoprobe showed high MR signal enhancement (SE), relatively stable NIR FL intensity upon 808 nm laser irradiation, sensitive PA response and strong photothermal–photodynamic injury ability to the cancer cells, proving the remarkable performance in multimodal imaging and therapy. Therefore, the proposed aggregation and crosslinking assembly strategy and the designed highly efficient multifunctional nanoprobe are promising for the development of high-relaxivity T_1 CAs and cancer theranostics.

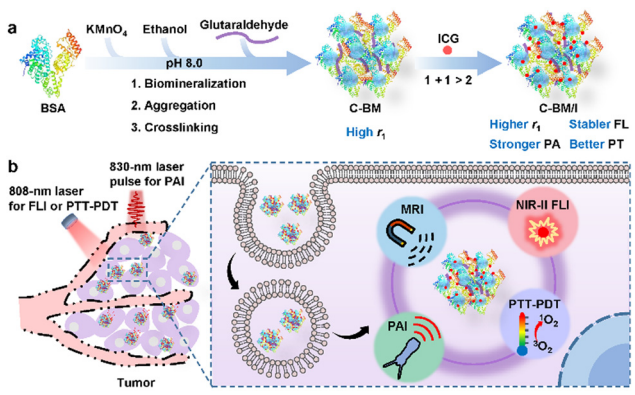

Scheme 1 General design of C-BM with sensitized relaxivity and C-BM/I for *in vivo* multimodal imaging and phototherapy (PTT-PDT). (a) Synthetic route of BM, C-BM and C-BM/I along with r_1 change and improved performance. (b) Cartoon illustration of C-BM/I transfection for *in vivo* T_1-weighted MRI, NIR-II FLI, PAI and PTT-PDT of H460 tumors.

Experimental

General experiments

The materials, reagents, apparatus, *in vitro* PA imaging, evaluation of photothermal conversion efficiency, cell culture and cellular uptake of C-BM/I, colocalization imaging, *in vitro* singlet oxygen generation, cytotoxicity detected with CCK-8, cell viability detected with Calcein AM/PI staining, flow cytometric analysis, animals and tumor models, *in vivo* photothermal–photodynamic therapy and histopathological analysis are presented in the ESI.†

Preparation of albumin–manganese-based nanocomposites

C-BM was synthesized by a facile method referring to the fabrication processes of BSA-MnO_2 (BM) nanoparticles[13,14] and human serum albumin (HSA) nanoparticles[25,26] with some modifications. In brief, BSA (60 mg) was dissolved in PB (pH 8.0, 2 mL), and 40 μL of $KMnO_4$ solution (20 mg mL^{-1}) was then added dropwise with vigorous stirring at 1000 rpm. After stirring for 1 h at room temperature, the yellowish-brown BM solution was acquired. After ethanol (2 mL) was carefully added to the above solution at a rate of 1 mL min^{-1} with continuous stirring at 1000 rpm, 8% glutaraldehyde (60 μL) was added into the mixture, which was kept stirring for another 12 h, and then ultrafiltrated five times (3000 g, 10 min) with a centrifugal filter device (MWCO = 100 kDa) at 4 °C to obtain C-BM solution. During ultrafiltration phosphate anions, ethanol and excess glutaraldehyde could be removed. For comparison, C-BM-1 or C-BM-2 without the introduction of ethanol or glutaraldehyde was synthesized with the same method. Uncross-linked BM was also synthesized as the above except a subsequent desolvation and cross-linking process, and dialyzed against DI water in a dialysis bag (MWCO = 1000 Da) for 24 h to remove phosphate anions. The Mn concentrations in the

obtained C-BM and uncross-linked BM solution were determined with ICP-AES to be 1.8 and 0.9 mM, respectively.

C-BM/I was prepared through the strong hydrophobic interactions between C-BM and ICG. Specifically, ICG (4 mg) was added into the as-prepared C-BM solution (2 mL). After stirring at 4 °C for 12 h in the dark, the C-BM/I solution was obtained.

Multimodal imaging of cell pellets

After H460 cells (~3×10^6 cells per well) were seeded on a cell culture dish (60 × 12 mm) by the above culture procedure overnight, the cells were incubated with 2 mL of fresh medium containing BM, C-BM, ICG or C-BM/I (40 μg mL^{-1} [ICG], 0.036 mM [Mn]) for different times, and then washed twice with PBS to trypsinize with 0.5 mL trypsin. The cell pellets were collected after centrifugation at 1000 rpm to take NIR-II fluorescence images with 808 nm excitation, 1300 nm long-pass (LP) filter and 30 ms exposure time, T_1-weighted MR images with an acquisition time of 685 s, and PA images with 830 nm excitation. The signal-to-background ratio (SBR) of NIR-II FL imaging and the MR signal enhancement (SE, 100%) were calculated from SI/SI_0 and $[(SI - SI_0)/SI_0] \times 100\%$, respectively, where SI is the signal intensity and SI_0 is the signal intensity at 0 h.

In vivo multimodal imaging

After H460 tumor-bearing nude mice were intratumorally (i.t.) injected with BM, C-BM, ICG or C-BM/I (0.09 mM [Mn], 100 μg mL^{-1} [ICG]) dispersed in 100 μL normal saline for different times, and *in vivo* multimodal imaging was performed with the following procedures.

For T_1-weighted MR imaging, the BM-, C-BM- or C-BM/I-treated mice were scanned in the tail-prone position with an acquisition time of 685 s. RadiAnt DICOM Viewer was used for the readout of signal intensity (SI) at each time point before (t = 0) and after injection of nanocomposites.

For NIR-II fluorescence imaging, the ICG- or C-BM/I-treated tumors were immediately irradiated with an 808 nm laser (0.33 W cm^{-2}) for 10 min. The whole body NIR-II FL images were collected during irradiation and after irradiation for 0.5 h to 24 h with 808 nm excitation, 10 W laser power, 1300 nm long-pass filter, and an exposure time of 150 ms. The fluorescence intensity in the region of interest (ROI) was read out using Image J software.

The PA images of ICG or C-BM/I-treated tumors were acquired with excitation at 830 nm. The PA intensity in the tumor at each time point was quantified by ROI measurement using the equipped software of the imaging system. PA average thresh (the average of PA signals within top 10% in ROI) was used for *in vivo* data analysis.

Results and discussion

Characterization of C-BM

After a $KMnO_4$ solution was added dropwise in BSA solution for 1 h, yellowish-brown colloidal dispersion was produced due to the oxidation of BSA by $KMnO_4$ (Fig. S1 and S2, ESI†), which showed spherical-like morphology of BSA-MnO_2 with 3.2 nm in diameter (Fig. 1a), consistent with the previous report.[13,14] The addition of ethanol led to the formation of BM aggregates due to the desolvation effect, and then crosslinking *via* the aldimine condensation reaction between aldehyde groups of glutaraldehyde and amino groups of BM aggregates to produce stable C-BM nanoaggregates (Fig. S1, ESI†), which led to an orange colloidal dispersion (Fig. S2, ESI†) and significant nanoaggregates up to hundreds of nanometers without obvious change in individual nanoparticle size (Fig. 1b). The presence and distribution of Mn and O elements in C-BM could be confirmed by energy dispersive spectroscopic (EDS) elemental mapping images (Fig. 1c), EDS spectrum (Fig. S3, ESI†) and EDS line profiles (Fig. S4, ESI†). The hydrodynamic size of C-BM was mainly at ~317 nm, which was significantly greater than that of BM (~7.4 nm), further proving the aggregation & crosslinking process (Fig. S5, ESI†). The aggregation and crosslinking also led to the increase of negative zeta potential (Fig. S6, ESI†), indicating less amino groups on the C-BM surface.

BM exhibited a strong characteristic absorption peak of protein at around 280 nm (Fig. 1d), proving the existence of BSA. However, the characteristic absorption peak of BSA in C-BM was significantly blue-shifted to 267 nm, which could be attributed to the slight structure changes of BSA after the aggregation and crosslinking process. Comparatively, there were no significant changes in the weak absorption of MnO_2 at 300–400 nm (Fig. 1d),[27,28] and the amide I and II bands of

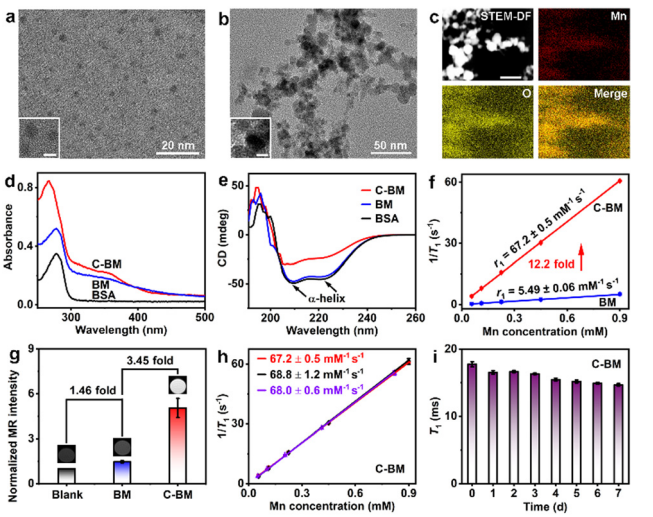

Fig. 1 Characterization of C-BM. TEM images of (a) BM and (b) C-BM. Inset: Corresponding HRTEM images. Scale bar: 5 nm. (c) Scanning transmission electron microscopy dark field (STEM-DF) and EDS elemental mapping images of C-BM. Scale bar: 25 nm. (d) UV-Vis absorption spectra of BSA, BM and C-BM. (e) CD spectra of BSA, BM and C-BM dispersed in PBS (pH 7.4). (f) Plots of $1/T_1$ of BM and C-BM at 0.5 T *versus* Mn concentration in the solution. (g) T_1-weighted MR images and intensity of BM and C-BM solution (0.056 mM [Mn]) at 1.0 T (Blank = H_2O). (h) Plots of $1/T_1$ of C-BM at 0.5 T *versus* Mn concentration, from 3 batches of C-BM samples. (i) T_1 relaxation times of protons in C-BM solution (0.9 mM [Mn]) at 0.5 T after storage at 4 °C for 0 to 7 days. Error bars represent standard deviation (SD, n = 3).

BSA at 1653 and 1531 cm^{-1} (Fig. S7, ESI†),[29,30] indicating the presence of MnO_2 nanoparticles and amide bonds of BSA in C-BM. The CD spectrum of BM showed two negative peaks at 208 and 222 nm, which were the same as those of BSA, while C-BM showed an obvious attenuated intensity of these peaks (Fig. 1e). Thus, the oxidation of BSA by $KMnO_4$ had negligible influence on the α-helix structures of BSA,[31] while the aggregation and crosslinking obviously impacted the secondary structure of BSA. The former was significantly different from previous reports, in which the oxidation changed the secondary structure of BSA.[13] This result could be attributed to the significantly lower molar ratio of $KMnO_4$ to BSA for BM synthesis (Table S1, ESI†). The X-ray photoelectron spectroscopic (XPS) spectra of BM and C-BM suggested the presence of O, N and C elements at 531 eV, 399 eV and 285 eV, respectively (Fig. S8, ESI†). However, they did not show an obvious signal of Mn element, indicating its low contents in these nanocomposites, which were detected with inductively coupled plasma atomic emission spectrometry (ICP-AES) to be 0.34% and 0.35%, respectively. The Mn content was 8.2–11.1 fold lower than those in the reported BMs due to the lower molar ratio of $KMnO_4$ to BSA (Table S1, ESI†). Additionally, the slight difference in the Mn contents of BM and C-BM could be attributed to their different purification methods.

The reciprocal of T_1 relaxation time of protons in both BM and C-BM solutions showed a linear increase with increasing Mn concentration (Fig. 1f). The T_1 relaxivity of BM and C-BM was thus obtained from the slope to be 5.49 ± 0.06 and 67.2 ± 0.5 mM^{-1} s^{-1}, respectively. The former was almost in accordance with the values reported previously,[13,14] but the latter was 12.2-fold higher than that of BM, indicating obvious sensitization of the aggregation and crosslinking to T_1 relaxivity of BM. The T_1 relaxivity of C-BM was also 8.5- or 11.4-fold higher than those of the previous BM with significantly higher Mn content (2.8% or 3.76%) at 0.5 T,[13,14] and higher than those of other AMNs at similar magnetic flux densities (MFD) (Table S1, ESI†).[15,16] Compared to Mn_xO_y or Mn_xO_y-based nanocomposites at higher MFD, the T_1 relaxivity of C-BM at 0.5 T was also sufficiently outstanding (Table S2, ESI†). Besides, the sensitization in T_1 relaxivity of BM was much stronger than those of Gd^{3+}-based nanoassemblies (Table S3, ESI†).[20–22] The control C-BM-1 and C-BM-2 without the introduction of ethanol or glutaraldehyde both showed obvious increase in hydrodynamic size compared to BM (Fig. S9, ESI†), indicating ethanol induced aggregation and glutaraldehyde induced crosslinking. The T_1 relaxivity of C-BM-1 and C-BM-2 was obtained to be 37.4 ± 0.2 and 17.0 ± 0.2 mM^{-1} s^{-1} respectively, about 6.8- and 3.1-fold higher than that of BM. These results confirmed that both the aggregation and crosslinking were contributed to the sensitization to T_1 relaxivity of BM, which resulted from the prolonged tumbling time of paramagnetic centers due to the significantly increased size[5,23] and the improved hydrophilic ability and water exchange rate due to the hydrophilic BSA modification of higher density around paramagnetic centers.[13,32] The high r_1 of C-BM with good repeatability provided a powerful tool for T_1-weighted MRI, which showed 3.45-fold increase of MR intensity compared to BM at the same Mn concentration (Fig. 1g and h). In addition, the T_1 relaxation time of protons in C-BM solution during storage was also stable (Fig. 1i), and the C-BM did not aggregate in generally used media (Fig. S10, ESI†), indicating excellent solubility and satisfactory colloidal stability under physiological conditions. Therefore, C-BM was an outstanding T_1 CA with low Mn content and high relaxivity, showing the tremendous potential for *in vivo* MR imaging at a low dose.

Characterization and *in vitro* performance of C-BM/I

After loading ICG into C-BM through strong hydrophobic interactions,[13,33,34] the colloidal dispersion of C-BM/I became dark-green (Fig. S2, ESI†). The obtained C-BM/I showed a hydrodynamic diameter of ~309 nm (Fig. S11a, ESI†) and favorable colloidal stability in different media (Fig. S11b, ESI†). The slight decrease in the hydrodynamic size of C-BM/I compared to C-BM was due to slightly increased temperature and accelerated nanoparticle motion of C-BM/I during the test, which was caused by the absorption of C-BM/I at 633 nm. Although ICG is a negatively charged molecule with two sulfonic groups, the Zeta potential of C-BM/I did not obviously change in comparison with that of C-BM (Fig. S6, ESI†), indicating that the loaded ICG molecules entered into the interior hydrophobic cavities of C-BM rather than the surface.

The T_1 relaxivity of C-BM/I was obtained to be 97.3 ± 0.3 mM^{-1} s^{-1} (Fig. 2a), which was ~1.45-fold higher than that of C-BM, revealing the facilitation of the ICG loading to T_1 relaxivity of AMNs.[13] This could be attributed to the prolonged tumbling time due to the increased weight of nanocomposites, and the improved water exchange rate in the presence of amphiphilic ICG.[13] Predictably, the T_1 relaxation time of protons in C-BM/I solution (10–12 ms) was lower than that in C-BM solution (14–18 ms) (Fig. S12, ESI† and Fig. 1i), leading to a brighter MR image at the same Mn concentration (Fig. 2a, inset). Compared to C-BM, the stability of T_1 relaxation time of C-BM/I solution during storage was also slightly improved.

ICG has been widely used for NIR-I FLI (700–900 nm)[35,36] and NIR-II FLI (1000–1700 nm).[37,38] In these wavelength ranges, the C-BM/I showed NIR-I FL centered at ~801 nm with 665 nm excitation (Fig. S13, ESI†), and NIR-II FL tail with 808 nm excitation, which was capable of NIR-II FL imaging even under a 1300 nm LP filter (Fig. S14, ESI†). The NIR-II FL intensity of free ICG showed continuous decline upon 808 nm laser irradiation due to its photobleaching characteristic even at 808 nm excitation (Fig. 2b). After ICG was loaded into C-BM, the FL intensity became relatively stable (Fig. 2c). At the same ICG concentration, the weaker initial FL intensity of C-BM/I was due to the aggregation-caused quenching (ACQ) effect of ICG within C-BM/I. Different from 1.95-fold FL intensity decrease of free ICG at 1000 nm after 10 min irradiation, the FL intensity of C-BM/I showed a 1.21-fold increase (Fig. 2d). The slightly increased FL intensity could be probably attributed to the release of a few ICG within C-BM/I due to the deformation of albumin under laser-induced hyperthermia.[39] The different changes could be also observed from the NIR FL images

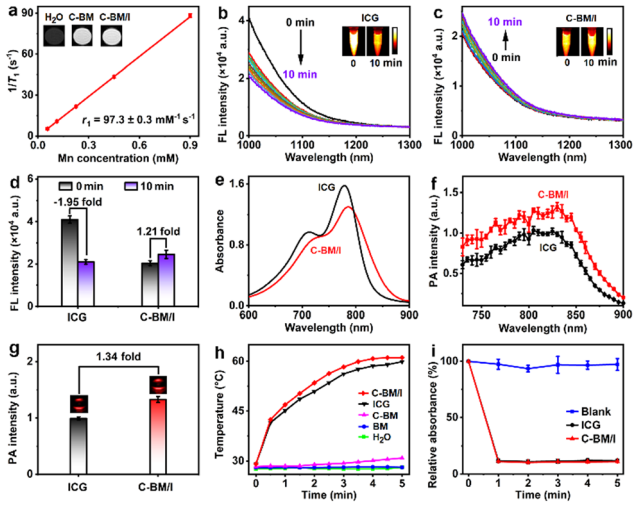

Fig. 2 T_1 relaxation, NIR-II FL, PA and PT properties of C-BM/I. (a) Plot of $1/T_1$ of C-BM/I at 0.5 T *versus* Mn concentration. Inset: T_1-weighted MR images at 0.056 mM [Mn] and 1.0 T. NIR-II FL spectra of (b) ICG and (c) C-BM/I (12.5 μg mL^{-1} [ICG]) during 808 nm laser irradiation (0.33 W cm^{-2}) for 0 to 10 min with 808 nm excitation. Inset: NIR FL images collected with 900 nm LP filter and exposure time of 10 ms at 0 and 10 min irradiation. (d) FL intensity of ICG and C-BM/I at 1000 nm before and after 10 min irradiation. (e) Vis-NIR absorption and (f) PA spectra of C-BM/I and ICG (10 μg mL^{-1} [ICG]). (g) PA images and intensity of C-BM/I and ICG (10 μg mL^{-1} [ICG]) with 830 nm excitation. (h) Time-dependent temperature of BM, C-BM, ICG and C-BM/I (80 μg mL^{-1} [ICG], 0.072 mM [Mn]) upon 808 nm irradiation (0.33 W cm^{-2}). (i) Time-dependent relative absorbance (%) of DPBF at 412 nm for blank, ICG and C-BM/I (5 μg mL^{-1} [ICG]) under 808 nm irradiation (0.33 W cm^{-2}). DPBF alone was used as blank. Error bars are SD (n = 3).

(Fig. 2b and c, inset), showing the superiority of C-BM/I against laser irradiation.

The absorption spectrum of free ICG showed two NIR absorption peaks at 715 and 779 nm, which was red-shifted to 725 and 786 nm respectively after ICG was loaded into C-BM (Fig. 2e). The loading slightly decreased the absorption intensity of ICG, and improved its storage stability in solution (Fig. S15, ESI†). After 17 days free ICG produced a new absorption peak at ~889 nm due to its structure change, while C-BM/I solution did not show obvious change in the absorption peak position and intensity. Different from the decrease of absorption intensity, the loading led to the red-shift of the maximum PA peak from ~805 nm to ~830 nm and the improvement of PA intensity (Fig. 2f), and the PA signal at 830 nm of C-BM/I was about 1.34-fold higher than that of free ICG (Fig. 2g), indicating the facilitation of C-BM to the PA effect of ICG. The promotion was presumably due to the partial aggregation of ICG in C-BM[40,41] and could be further verified from the linear correlations of the PA signal of C-BM/I to ICG concentration (Fig. S16, ESI†), which showed a slope of 0.0747, about 1.31-fold higher than 0.0571 of free ICG. Therefore, the C-BM/I with low Mn content provided a resultful PA contrast agent for bioimaging of deep-seated tissues.

The PA effect induced by thermoelastic expansion upon a pulsed laser often accompanied with a photothermal effect.[42,43] In order to achieve the theranostics of cancer, the photothermal performance of C-BM/I was further examined. Under 808 nm irradiation (0.33 W cm^{-2}), the temperature of C-BM/I solution (80 μg mL^{-1} [ICG], 0.072 mM [Mn]) increased gradually and reached 61.1 °C at 5 min, while the temperature of 80 μg mL^{-1} ICG was 59.9 °C, and the control groups including H_2O, BM and C-BM did not exhibit an obvious temperature increase (Fig. 2h and Fig. S17, ESI†). The slightly higher temperature of C-BM/I under 808 nm irradiation was also due to the partially aggregated ICG, which led to increased non-radiative transition to release more heat (Fig. 2e).[44,45] It was predictable that the temperature elevation positively depended on the C-BM/I concentration and laser power density (Fig. S18, ESI†). At the power density of 0.99 W cm^{-2}, the temperature of C-BM/I solution (80 μg mL^{-1} [ICG]) could even reach ~107.8 °C after 5 min irradiation. The photothermal conversion efficiency (PCE) of C-BM/I was calculated to be 16.0%, slightly higher than that of ICG (14.3%) (Fig. S19, ESI†). These values were basically consistent with previous reports (Table S4, ESI†).[46–49] Besides, ICG could induce the formation of singlet oxygen ($^1O_2$) under NIR laser irradiation for PDT.[50,51] Consequently, during 808 nm irradiation for 5 min, significant $^1O_2$ generation in C-BM/I was also demonstrated by the rapid decrease of DPBF characteristic absorbance at 412 nm, showing favorable PDT efficiency of C-BM/I comparable to ICG (Fig. 2i and Fig. S20, ESI†). Therefore, C-BM/I was an excellent phototherapeutic probe for cancer PTT-PDT along with multimodal imaging.

NIR-II FLI, T_1-weighted MRI and PAI of cell pellets and photothermal–photodynamic lethality of cells

The cellular uptake of C-BM/I in human NCI-H460 lung cancer cells was firstly examined with confocal FL imaging at 665 nm excitation. The FL intensity of ICG in H460 cells increased gradually during incubation with C-BM/I, and reached the maximum intensity at ~4 h (Fig. S21, ESI†), at which the colocalization experiment confirmed the distribution of C-BM/I in the lysosomes (Fig. S22, ESI†), indicating that C-BM/I was endocytosed into the lysosomes of H460 cells.

After ICG or C-BM/I was endocytosed into H460 cell pellets, the cell pellets became dark green (Fig. 3a). The NIR-II FL images with 1300 nm LP filter showed that the FL of cell pellets gradually enhanced during ICG or C-BM/I incubation for 0.5–6 h (Fig. 3a), and the signal-to-background ratio (SBR) reached the peak value at ~6 h (Fig. 3b), which was slightly longer than the maximum cellular uptake time. The difference in the times reaching peak values resulted from the significantly more cells used in NIR-II FL imaging of cell pellets than those in confocal FL imaging of cells. The decrease in NIR-II FL intensity after 6 h incubation was probably caused by the metabolism of endocytosed probes in cells. As observed in solution, the NIR-II FL intensity of C-BM/I-treated cell pellets was also relatively weaker than that of ICG-treated cell pellets.

After incubating H460 cell pellets with BM-, C-BM- or C-BM/I for 0.5 h, they showed bright MR contrast (Fig. 3c), proving the efficient cellular uptake of these nanocomposites. The MR SEs of C-BM-treated (69.9%) and C-BM/I-treated (77.2%) cell pellets

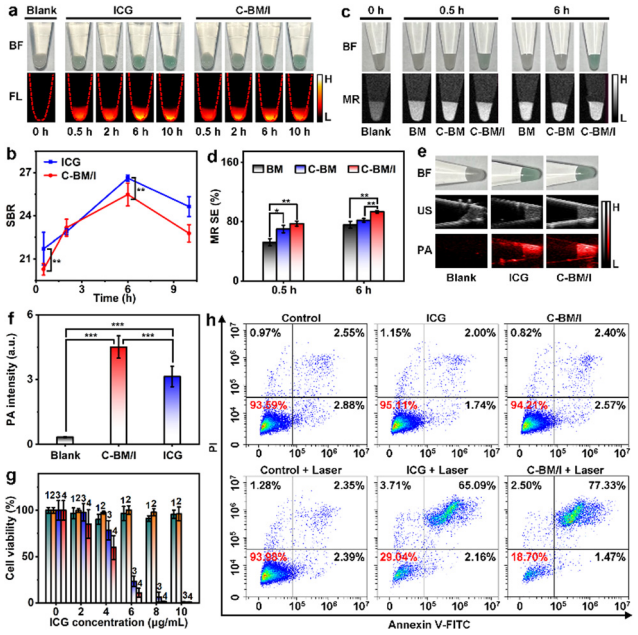

Fig. 3 NIR-II FLI, T_1-weighted MRI, PAI and PTT-PDT of H460 cells. (a) Bright field (BF) and NIR-II FL images and (b) SBRs of cell pellets after incubation with ICG or C-BM/I for different times (n = 3). (c) BF and MR images and (d) MR SE of cell pellets after incubation with BM, C-BM or C-BM/I for 0.5 and 6 h (n = 3). (e) BF, ultrasonic (US), PA images and (f) PA intensity of cell pellets after incubation with ICG or C-BM/I for 6 h (n = 3). The cell pellets without treatment were used as blank, [ICG] = 40 μg mL^{-1}, and [Mn] = 0.036 mM. (g) Cell viability after incubation with ICG (1,3) or C-BM/I (2,4) without (1,2) or with (3,4) 808 nm irradiation (0.77 W cm^{-2}, 5 min) (n = 4). (h) Flow cytometric analysis of H460 cells before and after incubation with C-BM/I or ICG (6 μg mL^{-1} [ICG]) without or with 808 nm laser (0.77 W cm^{-2}, 5 min) using Annexin V-FITC/PI staining. The cells without treatment were used as control. Error bars are SD. Statistical significance was calculated by Student's t-test (NS, not significant, *$p < 0.05$, **$p < 0.01$ and ***$p < 0.001$).

were higher than that of BM-treated (52.3%) cell pellets (Fig. 3d). After 6 h incubation, the MR SEs of BM-, C-BM- and C-BM/I-treated cell pellet significantly increased to 75.6%, 81.7% and 93.2%, respectively, indicating more endocytotic probes in the cells.

After 6 h incubation of H460 cell pellets with ICG or C-BM/I, these cell pellets exhibited obvious PA signals at 830 nm compared with the blank group (Fig. 3e). The PA intensity of C-BM/I-treated cell pellets was ~1.44-fold higher than that of ICG-treated cell pellets (Fig. 3f), implying better PA imaging ability of C-BM/I than ICG at 830 nm excitation due to the facilitation of C-BM to ICG.

The photothermal–photodynamic lethality of ICG- or C-BM/I-treated H460 cells under 808 nm laser irradiation (0.77 W cm^{-2}) was also examined. Obvious intracellular green fluorescence in C-BM/I-treated cells comparable to ICG-treated cells was firstly observed under irradiation, while no significant fluorescence occurred in other groups, which proved the efficient $^1O_2$ generation during phototherapy (Fig. S23, ESI†). In the absence of laser irradiation, both ICG and C-BM/I showed negligible cytotoxicity to H460 cells (Fig. 3g), indicating good biocompatibility. However, their dose-dependent cytotoxicity was observed under 808 nm laser irradiation. The lower cell viability of C-BM/I-treated cells compared with ICG-treated cells (Fig. 3g) demonstrated the improved photothermal–photodynamic lethality of C-BM/I due to its slightly stronger temperature elevation ability (Fig. 2h and Fig. S17, ESI†). The higher photothermal–photodynamic lethality was further verified by the flow cytometric analysis (Fig. 3h) and fluorescence staining of live and dead cells with Calcein AM and propidium iodide (Fig. S24, ESI†). At the same ICG concentration the cell apoptosis rate of C-BM/I-treated cells (78.80%) was higher than that of ICG-treated cells (67.25%) under laser irradiation (Fig. 3h), demonstrating an efficient tumor PTT-PDT nanoprobe.

In vivo T_1-weighted MRI, NIR-II FLI and PAI of H460 tumors

Subcutaneous (s.c.) H460 tumor xenograft nude mice were used to examine the *in vivo* multimodal imaging abilities of BM, C-BM and C-BM/I. After intratumoral (i.t.) injection of BM, C-BM or C-BM/I with the same Mn amount into H460 tumor-bearing mice, bright MR contrast was observed in tumors (Fig. 4a). At 1 h post injection, the MR SE of C-BM/I-treated tumor reached ~129.5%, which was nearly the same as that of C-BM-treated tumors and ~2.2-fold higher than that of BM-treated tumors, proving the sensitization to T_1 relaxivity by aggregation and crosslinking assembly to shorten the T_1 relaxation time of protons in tumors. The continuous decrease of MR SE was observed after 2 h post injection (Fig. 4b), which could be attributed to the metabolism of probes in tumors, as observed in cells. The higher MR SE of the C-BM/I-treated tumor compared with the C-BM-treated tumor at 12 h and 24 h was due to the slower metabolic rate of C-BM/I with increased weight.

The *in vivo* NIR-II FLI was performed with a 1300 nm LP filter, with which an extremely low fluorescence background could be achieved (Fig. S25, ESI†). After i.t. injection of ICG or C-BM/I into tumor-bearing mice, the tumors showed bright FL (Fig. 4c). The FL intensity of ICG-treated tumor at 2 min was ~23.1% higher than that of the C-BM/I-treated tumor, as observed in solution and cell pellets. However, 808 nm laser irradiation (0.33 W cm^{-2}) increased the FL intensity of C-BM/I-treated tumor due to the thermally induced release of few ICG (Fig. 4d), which led to a similar FL intensity with ICG-treated tumor after 808 nm laser irradiation (0.33 W cm^{-2}) for 10 min. Notably, obvious NIR-II FL also appeared in the livers of ICG- and C-BM/I-treated mice at 2–10 min, and then moved to the intestine sites, showing the *in vivo* metabolism process of probes from the liver to the intestine. The slower metabolic rate of C-BM/I compared with free ICG in tumors made the NIR-II FL significantly stronger after 0.5–4 h post injection with 10 min irradiation (Fig. 4c and e). After 12 h post injection both C-BM/I- and ICG-treated tumors showed very low FL intensity, further demonstrating the *in vivo* metabolism of probes.

The PA images of the C-BM/I-treated tumor showed enhanced PA signals at 830 nm excitation compared with the ICG-treated tumor (Fig. 4f), indicating the *in vivo* facilitation of C-BM. The PA signals were much stronger than those from the

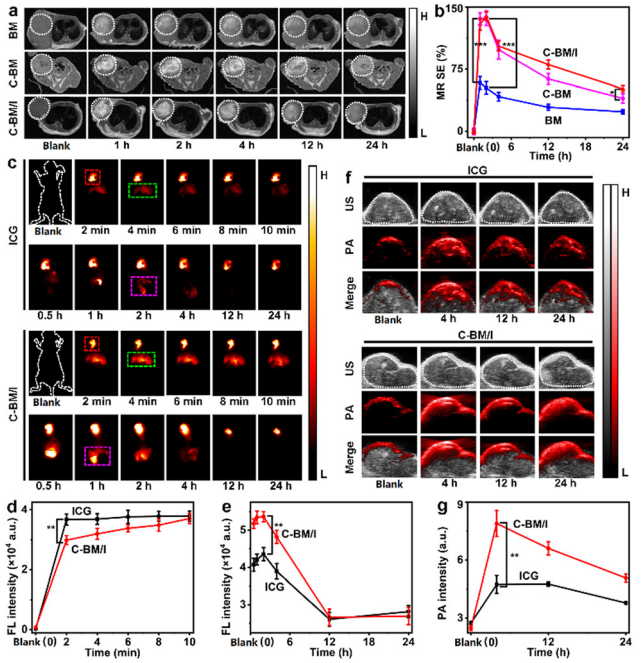

Fig. 4 T_1-Weighted MRI, NIR-II FLI and PAI of H460 tumor-bearing mice. (a) MR images and (b) MR SE of tumors before and after injection of BM, C-BM or C-BM/I for different times. (c) NIR-II FL images and (d and e) intensity of mice before and after injection of ICG or C-BM/I for different times with 808 nm laser irradiation (0.33 W cm^{-2}) in the initial 10 min. Red, green and magenta boxes indicate tumor, liver and intestine sites, respectively. (f) PA images and (g) intensity of tumors before and after injection of ICG or C-BM/I for different times. The injection amount of BM, C-BM, ICG or C-BM/I was 100 μL saline containing 0.09 mM [Mn] or 100 μg mL^{-1} [ICG]. Error bars are SD (n = 3). Statistical significance was calculated by Student's t-test (*p < 0.05, **p < 0.01 and ***p < 0.001).

optical absorption of fur and skin tissues prior to probe injection. At 4 h post injection, the PA intensity of the C-BM/I-treated tumor was ~1.66-fold higher than that of the ICG-treated tumor (Fig. 4g). Similarly, the metabolism of probes in the tumor resulted in the decrease of PA intensity. Therefore, C-BM/I showed a satisfactory performance in multimodal imaging including T_1-weighted MRI, NIR-II FLI and PAI to provide guidance for cancer PTT-PDT.

In vivo cancer PTT-PDT with C-BM/I

At 2 h post injection of saline, ICG or C-BM/I (80 μg mL^{-1} [ICG], 50 μL), the H460 tumor-bearing mice were used for real-time thermal imaging under 808 nm irradiation (0.55 W cm^{-2}). As shown in Fig. 5a and b, the maximum temperature of the C-BM/I-treated tumor could reach 51.5 °C during 5 min irradiation, which was enough for *in vivo* PTT,[52–54] while the maximum temperatures of ICG-and saline-treated tumors were 46.6 °C and 41.1 °C, respectively. The difference of ~4.9 °C between C-BM/I- and ICG-treated tumors was close to that between C-BM/I (72.4 °C) and ICG (68.2 °C) solution under identical conditions (Fig. S26, ESI†), ensuring the better PTT efficacy of C-BM/I.

The *in vivo* PTT-PDT efficacy of C-BM/I with 5 min irradiation at 808 nm and 0.55 W cm^{-2} was examined through

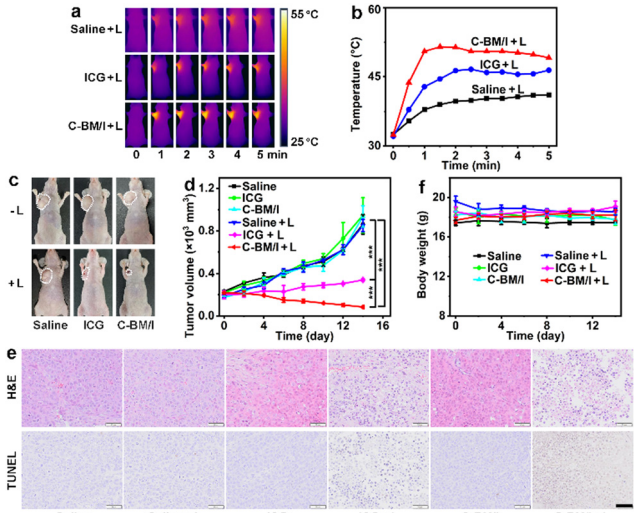

Fig. 5 PTT-PDT of H460 tumor-bearing mice. (a) Photothermal images and (b) time-dependent temperature of tumors under 808 nm laser irradiation (0.55 W cm^{-2}, 5 min) at 2 h post injection of 50 μL normal saline, ICG or C-BM/I (80 μg mL^{-1} [ICG]). (c) Representative photographs of mice with six treatments at day 14. (d) Tumor volumes at 0–14 days post treatments. (e) H&E and terminal deoxynucleotidyl transferase dUTP nick-end labeling (TUNEL) staining of tumor slices from mice at day 14 post treatments. Scale bar: 50 μm. (f) Body weight of mice at 0–14 days post treatments. L = 808 nm irradiation. Error bars are SD (n = 3). Statistical significance was calculated by Student's t-test (***p < 0.001).

monitoring the tumor sizes of mice with different treatments. In the absence of irradiation, the time-depended tumor sizes did not show obvious differences among saline, ICG and C-BM/I treatments (Fig. 5c). However, the C-BM/I-treated tumor with 5 min irradiation showed significantly smaller size (Fig. 5d), demonstrating remarkably stronger inhibition of C-BM/I on tumor growth, which led to significantly more cell death (Fig. 5e). Moreover, the body weights of these mice did not apparently change after the treatments (Fig. 5f), indicating little side effect of probes, which was further verified from the hematoxylin and eosin (H&E) staining images of major mouse organs such as the heart, liver, spleen, lung and kidney of the mice with saline injection and C-BM/I plus irradiation treatments (Fig. S27, ESI†).

Conclusions

An aggregation and crosslinking assembly strategy is proposed for constructing high-relaxivity albumin–manganese nanocomposites C-BM with low Mn content. This strategy results in an ~12.2-fold increase of T_1 relaxivity of BM at a Mn content of 0.35%, which is much higher than those of previously reported BMs with 10 times Mn content, demonstrating an excellent sensitizing effect to T_1 relaxivity of AMNs. Moreover, the further increase of T_1 relaxivity by ~1.45 fold is achieved after ICG loading to produce C-BM/I, which also exhibits more stable NIR-II FL against 808 nm laser irradiation, stronger PA signal and a better photothermal effect than ICG, proving a merit of "1 + 1 > 2". C-BM/I possesses good biocompatibility, and can

be used for sensitive T_1-weighted MR, NIR-II FL and PA multimodal imaging and highly efficient cancer PTT-PDT with little side effects. This work presents a new paradigm for the preparation of high-relaxivity T_1 contrast agent to achieve long-term safety, and a general scaffold for the design of multifunctional nanoprobes for cancer theranostics.

Author contributions

Ying An: Conceptualization, methodology, investigation, formal analysis, and writing-original draft. Weiwei Chen: visualization, data curation, and formal analysis. Yiran Li: data curation and formal analysis. Hongxia Zhao: data curation and formal analysis. Deju Ye: data curation and resources. Huipu Liu: validation and formal analysis. Kun Wu: validation and formal analysis. Huangxian Ju: supervision, project administration, writing-review & editing, and funding acquisition.

Conflicts of interest

There are no conflicts to declare.

Acknowledgements

This work was supported by the National Natural Science Foundation of China (21890741, 21827812).

References

1 S. Kunjachan, J. Ehling, G. Storm, F. Kiessling and T. Lammers, *Chem. Rev.*, 2015, **115**, 10907–10937.
2 B. R. Smith and S. S. Gambhir, *Chem. Rev.*, 2017, **117**, 901–986.
3 T.-H. Shin, Y. Choi, S. Kim and J. Cheon, *Chem. Soc. Rev.*, 2015, **44**, 4501–4516.
4 G. J. Strijkers, W. J. M. Mulder, G. A. F. Tilborg and K. Nicolay, *Anticancer Agents Med. Chem.*, 2007, **7**, 291–305.
5 D. Ni, W. Bu, E. B. Ehlerding, W. Cai and J. Shi, *Chem. Soc. Rev.*, 2017, **46**, 7438–7468.
6 Y. Cao, L. Xu, Y. Kuang, D. Xiong and R. Pei, *J. Mater. Chem. B*, 2017, **5**, 3431–3461.
7 J. Wahsner, E. M. Gale, A. Rodriguez-Rodriguez and P. Caravan, *Chem. Rev.*, 2019, **119**, 957–1057.
8 S. Anbu, S. H. L. Hoffmann, F. Carniato, L. Kenning, T. W. Price, T. J. Prior, M. Botta, A. F. Martins and G. J. Stasiuk, *Angew. Chem., Int. Ed.*, 2021, **60**, 10736–10744.
9 B. Ding, P. Zheng, P. Ma and J. Lin, *Adv. Mater.*, 2020, **32**, 1905823.
10 H. B. Na, J. H. Lee, K. An, Y. I. Park, M. Park, I. S. Lee, D.-H. Nam, S. T. Kim, S.-H. Kim, S.-W. Kim, K.-H. Lim, K.-S. Kim, S.-O. Kim and T. Hyeon, *Angew. Chem., Int. Ed.*, 2007, **46**, 5397–5401.
11 Z. Zhao, J. Bao, C. Fu, M. Lei and J. Cheng, *Chem. Mater.*, 2017, **29**, 10455–10468.
12 Z. Zhang and Y. Ji, *Nanoscale*, 2020, **12**, 17982–18003.
13 J. Pan, Y. Wang, H. Pan, C. Zhang, X. Zhang, Y.-Y. Fu, X. Zhang, C. Yu, S.-K. Sun and X.-P. Yan, *Adv. Funct. Mater.*, 2017, **27**, 1603440.
14 W. Hou, Y. Jiang, G. Xie, L. Zhao, F. Zhao, X. Zhang, S.-K. Sun, C. Yu and J. Pan, *Nanoscale*, 2021, **13**, 8531–8542.
15 B. Xiao, X. Zhou, H. Xu, B. Wu, D. Hu, H. Hu, K. Pu, Z. Zhou, X. Liu, J. Tang and Y. Shen, *ACS Nano*, 2018, **12**, 12682–12691.
16 B. Xiao, D. Li, H. Xu, X. Zhou, X. Xu, Y. Qian, F. Yu, H. Hu, Z. Zhou, X. Liu, J. Gao, N. K. H. Slater, Y. Shen and J. Tang, *Biomaterials*, 2021, **274**, 120893.
17 A. D. Gitler, A. Chesi, M. L. Geddie, K. E. Strathearn, S. Hamamichi, K. J. Hill, K. A. Caldwell, G. A. Caldwell, A. A. Cooper, J.-C. Rochet and S. Lindquist, *Nat. Genet.*, 2009, **41**, 308–315.
18 H. S. Thomsen, O. Svendsen and S. Klastrup, *Acad. Radiol.*, 2004, **11**, 38–44.
19 A. Natanzon, A. H. Aletras, L.-Y. Hsu and A. E. Arai, *Radiology*, 2005, **236**, 859–866.
20 R. Yan, Y. Hu, F. Liu, S. Wei, D. Fang, A. J. Shuhendler, H. Liu, H.-Y. Chen and D. Ye, *J. Am. Chem. Soc.*, 2019, **141**, 10331–10341.
21 R. An, X. Cheng, S. Wei, Y. Hu, Y. Sun, Z. Huang, H.-Y. Chen and D. Ye, *Angew. Chem., Int. Ed.*, 2020, **59**, 20636–20644.
22 Y. Hu, J. Zhang, Y. Miao, X. Wen, J. Wang, Y. Sun, Y. Chen, J. Lin, L. Qiu, K. Guo, H.-Y. Chen and D. Ye, *Angew. Chem., Int. Ed.*, 2021, **60**, 18082–18093.
23 G. Liang, J. Ronald, Y. Chen, D. Ye, P. Pandit, M. L. Ma, B. Rutt and J. Rao, *Angew. Chem., Int. Ed.*, 2011, **50**, 6283–6286.
24 Z. Zhang, A. F. Kolodziej, M. T. Greenfield and P. Caravan, *Angew. Chem., Int. Ed.*, 2011, **50**, 2621–2624.
25 S. Bae, K. Ma, T. H. Kim, E. S. Lee, K. T. Oh, E.-S. Park, K. C. Lee and Y. S. Youn, *Biomaterials*, 2012, **33**, 1536–1546.
26 Q. Chen, X. Liu, J. Zeng, Z. Cheng and Z. Liu, *Biomaterials*, 2016, **98**, 23–30.
27 K. Kai, Y. Yoshida, H. Kageyama, G. Saito, T. Ishigaki, Y. Furukawa and J. Kawamata, *J. Am. Chem. Soc.*, 2008, **130**, 15938–15943.
28 Y. Ling, D. Zhang, X. Cui, M. Wei, T. Zhang, J. Wang, L. Xiao and Y. Xia, *Angew. Chem., Int. Ed.*, 2019, **58**, 10542–10546.
29 E. Beilis, B. Belgorodsky, L. Fadeev, H. Cohen and S. Richter, *J. Am. Chem. Soc.*, 2014, **136**, 6151–6154.
30 R. Nandi, Y. Agam and N. Amdursky, *Adv. Mater.*, 2021, **33**, 2101208.
31 A. J. Miles and B. A. Wallace, *Chem. Soc. Rev.*, 2016, **45**, 4859–4872.
32 K. Liu, Z. Cai, X. Chi, B. Kang, S. Fu, X. Luo, Z.-W. Lin, H. Ai, J. Gao and H. Lin, *Nano Lett.*, 2022, **22**, 3219–3227.
33 L. Wang, H. Lin, X. Chi, C. Sun, J. Huang, X. Tang, H. Chen, X. Luo, Z. Yin and J. Gao, *Small*, 2018, **14**, 1801612.
34 Q. Chen, C. Liang, C. Wang and Z. Liu, *Adv. Mater.*, 2015, **27**, 903–910.
35 E. I. Altinoglu, T. J. Russin, J. M. Kaiser, B. M. Barth, P. C. Eklund, M. Kester and J. H. Adair, *ACS Nano*, 2008, **2**, 2075–2084.
36 C. Vinegoni, I. Botnaru, E. Aikawa, M. A. Calfon, Y. Iwamoto, E. J. Folco, V. Ntziachristos, R. Weissleder, P. Libby and F. A. Jaffer, *Sci. Transl. Med.*, 2011, **3**, 84ra45.

37 S. Zhu, Z. Hu, R. Tian, B. C. Yung, Q. Yang, S. Zhao, D. O. Kiesewetter, G. Niu, H. Sun, A. L. Antaris and X. Chen, *Adv. Mater.*, 2018, **30**, 1802546.
38 J. A. Carr, D. Franke, J. R. Caram, C. F. Perkinson, M. Saif, V. Askoxylakis, M. Datta, D. Fukumura, R. K. Jain, M. G. Bawendi and O. T. Bruns, *Proc. Natl. Acad. Sci. U. S. A.*, 2018, **115**, 4465–4470.
39 Y. Wan, G. Lu, J. Zhang, Z. Wang, X. Li, R. Chen, X. Cui, Z. Huang, Y. Xiao, J. Chelora, W. Zhang, Y. Liu, M. Li, H.-Y. Xie and C.-S. Lee, *Adv. Funct. Mater.*, 2019, **29**, 1903436.
40 J. Wu, L. You, S. T. Chaudhry, J. He, J.-X. Cheng and J. Mei, *Anal. Chem.*, 2021, **93**, 3189–3195.
41 Y. Yang, B. Chu, J. Cheng, J. Tang, B. Song, H. Wang and Y. He, *Nat. Commun.*, 2022, **13**, 1255.
42 L. Nie and X. Chen, *Chem. Soc. Rev.*, 2014, **43**, 7132–7170.
43 Y. Liu, P. Bhattarai, Z. Dai and X. Chen, *Chem. Soc. Rev.*, 2019, **48**, 2053–2108.
44 Q. Zou, M. Abbas, L. Zhao, S. Li, G. Shen and X. Yan, *J. Am. Chem. Soc.*, 2017, **139**, 1921–1927.
45 W. Du, Y. Chong, X. Hu, Y. Wang, Y. Zhu, J. Chen, X. Li, Q. Zhang, G. Wang, J. Jiang and G. Liang, *Adv. Funct. Mater.*, 2020, **30**, 1908073.
46 L. Yang, X. Hou, Y. Zhang, D. Wang, J. Liu, F. Huang and J. Liu, *J. Controlled Release*, 2021, **339**, 114–129.
47 X. Liu, N. Xu, X. Pu, J. Wang, X. Liao, Z. Huang and G. Yin, *J. Mater. Chem. B*, 2022, **10**, 4605–4614.
48 J. Zhang, K. Zhang, Y. Hao, H. Yang, J. Wang, Y. Zhang, W. Zhao, S. Ma and C. Mao, *J. Colloid Interface Sci.*, 2023, **633**, 679–691.
49 Q. You, Q. Sun, M. Yu, J. Wang, S. Wang, L. Liu, Y. Cheng, Y. Wang, Y. Song, F. Tan and N. Li, *ACS Appl. Mater. Interfaces*, 2017, **9**, 40017–40030.
50 P. Xue, M. Hou, L. Sun, Q. Li, L. Zhang, Z. Xu and Y. Kang, *Acta Biomater.*, 2018, **81**, 242–255.
51 P. Xue, R. Yang, L. Sun, Q. Li, L. Zhang, Z. Xu and Y. Kang, *Nano-Micro Lett.*, 2018, **10**, 74.
52 H. Shi, Y. Sun, R. Yan, S. Liu, L. Zhu, S. Liu, Y. Feng, P. Wang, J. He, Z. Zhou and D. Ye, *Nano Lett.*, 2019, **19**, 937–947.
53 X. Hu, Y. Tang, Y. Hu, F. Lu, X. Lu, Y. Wang, J. Li, Y. Li, Y. Ji, W. Wang, D. Ye, Q. Fan and W. Huang, *Theranostics*, 2019, **9**, 4168–4181.
54 S. Wang, L. Zhang, J. Zhao, M. He, Y. Huang and S. Zhao, *Sci. Adv.*, 2021, **7**, eabe3588.